[2] Y. Matsumura, H. Maeda, A new concept for macromolecular therapeutics in cancer chemotherapy: mechanism of tumoritropic accumulation of proteins and the antitumor agent Smancs, Cancer Res. 46 (1986) 6387–6392.
[3] H.M. Aliabadi, A. Lavasanifar, Polymeric micelles for drug delivery, Expert Opin. Drug Deliv. 3 (1) (2006) 130–162.
[4] N. Nishiyama, S. Okazaki, H. Cabral, M. Miyamoto, Y. Kato, Y. Sugiyama, K. Nishio, Y. Matsumura, K. Kataoka, Novel cisplatin-incorporated polymeric micelles can eradicate solid tumors in mice, Cancer Res. 63 (2003) 8977–8983.
[5] N. Nishiyama, M. Yokoyama, T. Aoyagi, T. Okano, Y. Sakurai, K. Kataoka, Preparation and characterization of self-assembled polymer–metal complex micelle from cis-dichlorodiammineplatinum(II) and poly(ethylene glycol)-poly(α,β-aspartic acid) block copolymer in an aqueous medium, Langmuir 15 (1999) 377–383.
[6] A. Bogdanov Jr, C. Martin, A.V. Bogdanova, T.J. Brady, R. Weissleder, An adduct of cis-diamminedichloroplatinum(II) and poly(ethylene glycol)poly(L-lysine)-succinate: synthesis and cytotoxic properties, Bioconjug. Chem. 7 (1) (1996) 144–149.
[7] R. Rebizak, M. Schaefer, E. Dellacherie, Polymeric conjugates of Gd^{3+}-diethylenetriaminepentaacetic acid and dextran. 1. Synthesis, characterization, and paramagnetic properties, Bioconjug. Chem. 8 (4) (1997) 605–610.
[8] M.M. Huber, A.B. Staubli, K. Kustedjo, M.H.B. Gray, J. Shih, S.E. Fraser, R.E. Jacobs, T.J. Meade, Fluorescently detectable magnetic resonance imaging agents, Bioconjug. Chem. 9 (2) (1998) 242–249.
[9] A. Bogdanov Jr, S.C. Wright, E.M. Marecos, A.V. Bogdanova, C. Martin, R. Weissleder, A long-circulating co-polymer in "passive targeting" to solid tumors, J. Drug Target. 4 (5) (1997) 321–330.
[10] R. Weissleder, A. Bogdanov Jr, C-H. Tung, H-J. Weinmann, Size optimization of synthetic graft copolymers for in vivo angiogenesis imaging, Bioconjug. Chem. 12 (2) (2001) 213–219.
[11] F. Ye, T. Ke, E-K. Jeong, X. Wang, Y. Sun, M. Johnson, Z-R. Lu, Noninvasive visualization of in vivo drug delivery of poly(L-glutamic acid) using contrast-enhanced MRI, Mol. Pharm. 3 (5) (2006) 507–515.
[12] X. Wen, E.F. Jackson, R.E. Price, E.E. Kim, Q. Wu, S. Wallace, C. Charnsangavej, J.G. Gelovani, C. Li, Synthesis and characterization of poly(L-glutamic acid) gadolinium chelate: a new biodegradable MRI contrast agent, Bioconjug. Chem. 15 (6) (2004) 1408–1415.
[13] Z-R. Lu, X. Wang, D.L. Parker, K.C. Goodrich, H.R. Buswell, Poly(L-glutamic acid) Gd (III)–DOTA conjugate with a degradable spacer for magnetic resonance imaging, Bioconjug. Chem. 14 (4) (2003) 715–719.
[14] Y. Wang, F. Ye, E-K. Jeong, Y. Sun, D.L. Parker, Z-R. Lu, Noninvasive visualization of pharmacokinetics, biodistribution, and tumor targeting of poly[N-(2-hydroxypropyl)methacrylamide] in mice using contrast enhanced MRI, Pharm. Res. 24 (6) (2007) 1208–1216.
[15] H. Kobayashi, M.W. Brechbiel, Dendrimer-based macromolecular MRI contrast agents: characterization and application, Mol. Imag. 2 (1) (2003) 1–10.
[16] H. Kobayashi, S. Kawamoto, S-K. Jo, H.L. Bryant Jr, M.W. Brechbiel, R.A. Star, Macromolecular MRI contrast agents with small dendrimers: pharmacokinetic differences between sizes and cores, Bioconjug. Chem. 14 (2) (2003) 388–394.
[17] H. Kobayashi, N. Sato, S. Kawamoto, T. Saga, A. Hiraga, T.L. Haque, T. Ishimori, J. Konishi, K. Togashi, M.W. Brechbiel, Comparison of the macromolecular MR contrast agents with ethylenediamine-core versus ammonia-core generation-6 polyamidoamine dendrimer, Bioconjug. Chem. 12 (1) (2001) 100–107.
[18] E. Nakamura, K. Makino, T. Okano, T. Yamamoto, M. Yokoyama, A polymeric micelle MRI contrast agent with changeable relaxivity, J. Control. Release 114 (2006) 325–333.
[19] V.P. Torchilin, PEG-based micelles as carriers of contrast agents for different imaging modality, Adv. Drug Deliv. Rev. 54 (2002) 235–252.
[20] G. Zhang, R. Zhang, X. Wen, L. Li, C. Li, Micelles based on biodegradable poly(L-glutamic acid)-b-polylactide with paramagnetic Gd ions chelated to the shell layer as a potential nanoscale MRI-visible delivery, Biomacromolecules 9 (1) (2008) 36–42.
[21] H.Y. Lee, H.W. Jee, S.M. Seo, B.K. Kwak, G. Khang, S.H. Cho, Diethylenetiramine-pentaacetic acid–gadolinium (DTPA–Gd)-conjugated polysuccinimide derivatives as magnetic resonance imaging contrast agents, Bioconjug. Chem. 17 (3) (2006) 700–706.
[22] N. Nasongkla, E. Bey, J. Ren, H. Ai, C. Khemtong, J.S. Guthi, S-F. Chin, A.D. Sherry, D.A. Boothman, J. Gao, Multifunctional polymeric micelles as cancer-targeted, MRI-ultrasensitive drug delivery systems, Nano Lett. 6 (11) (2006) 2427–2430.
[23] Z-R. Lu, F. Ye, A. Vaidya, Polymer platforms for drug delivery and biomedical imaging, J. Control. Release 122 (2007) 269–277.
[24] M. Yokoyama, G.S. Kwon, T. Okano, Y. Sakurai, M. Naito, K. Kataoka, Influencing factors on in vitro micelle stability of adriamycin-block copolymer conjugate, J. Control. Release 28 (1994) 59–65.
[25] Y. Takakura, T. Fujita, M. Hashida, H. Sezaki, Disposition character of macromolecules in tumor-bearing mice, Pham. Res. 7 (4) (1990) 330–346.
[26] A. Harada, K. Kataoka, Formation of polyion complex micelles in an aqueous milieu from a pair of oppositely-charged block copolymers with poly(ethylene glycol) segments, Macromolecules 28 (15) (1995) 5294–5299.

British Journal of Cancer (2009) 101, 1884–1890

www.bjcancer.com

Increase in tumour permeability following TGF-β type I receptor-inhibitor treatment observed by dynamic contrast-enhanced MRI

T Minowa[1], K Kawano[1], H Kuribayashi[2], K Shiraishi[3], T Sugino[4], Y Hattori[1], M Yokoyama[3] and Y Maitani*[,1]

[1]Institute of Medicinal Chemistry, Hoshi University, Ebara 2-4-41, Shinagawa, Tokyo 142-8501, Japan; [2]Varian Technologies Japan Limited, Shibaura 4-16-36, Minato, Tokyo 108-0023, Japan; [3]Kanagawa Academy of Science and Technology, Sakado 3-2-1, Takatsu, Kawasaki, Kanagawa 213-0012, Japan; [4]Department of Basic Pathology, Fukushima Medical University, Hikariga-oka 1, Fukushima 960-1295, Japan

BACKGROUND: To enhance the success rate of nanocarrier-mediated chemotherapy combined with an anti-angiogenic agent, it is crucial to identify parameters for tumour vasculature that can predict a response to the treatment of the anti-angiogenic agent.

METHODS: To apply transforming growth factor (TGF)-β type I receptor (TβR-I) inhibitor, A-83-01, to combined therapy, dynamic contrast-enhanced magnetic resonance imaging (DCE-MRI) was carried out in mice bearing colon 26 cells using gadolinium (Gd)-DTPA and for its liposomal formulation to evaluate changes in tumour microvasculature following A-83-01. Tumour vascular parameters from DCE-MRI were compared with histological assessment and *apparent diffusion coefficient* of water in tumour generated by diffusion-weighted MRI.

RESULTS: Contrary to evaluations reported for anti-angiogenic agents, A-83-01 treatment increased the initial area under the Gd concentration–time curve ($IAUGC_{60}$), volume transfer constant (K^{trans}) and fractional plasma volume (v_p) significantly within 24 h, that was positively related to α-smooth muscle actin-positive pericyte coverage and tumour cell proliferation, and was correlated inversely with the *apparent diffusion coefficient*. The vascular function of the tumour improved by A-83-01 treatment was well assessed on post-liposomal Gd-DTPA-enhanced MR images, which predicted delivery of a liposomal drug to the tumour.

CONCLUSION: These findings suggest that DCE-MRI and, in particular, K^{trans} and v_p quantitation, provide important additional information about tumour vasculature by A-83-01 treatment.

British Journal of Cancer (2009) **101,** 1884–1890. doi:10.1038/sj.bjc.6605367 www.bjcancer.com
Published online 3 November 2009

Keywords: MRI; liposome; angiogenesis; TGF-β inhibitor; contrast agent; tumour

The success of chemotherapeutic agents with solid tumours is critically dependant on the access that these agents have to the tumours via the so-called 'leaky vasculature'. In particular, tumour vasculature is crucial for the delivery of drugs encapsulated in nanocarriers (Matsumura and Maeda, 1986). Anti-angiogenesis effects are known to change the tumour vasculature; therefore, this technique has been already applied to combined therapy. Bevacizumab, an anti-vascular endothelial growth factor (VEGF) antibody, was developed for blocking angiogenesis and it is clinically used with other drugs to improve the efficiency of chemotherapy.

The roles of transforming growth factor (TGF)-β in cancer biology are complex; TGF-β can suppress or promote tumour growth depending on the type of cancer. Small molecule TGF-β type I receptor (TβR-I) inhibitor has a wide variety of effects (Jakowlew, 2006; Tsuchida *et al*, 2006). The TβR-I inhibitor LY364947 was reported to increase the accumulation of an anti-cancer drug encapsulated in nanocarriers by changing the micro-environmental vasculature (Kano *et al*, 2007). The TβR-I inhibitor A-83-01 is one of more potent inhibitors of TβR-I kinase/activin receptor-like kinase (ALK)-5 ($IC_{50} = 12$ nM) (Tojo *et al*, 2005) than a previously described ALK-5 inhibitors including LY364947 ($IC_{50} = 59$ nM) (Li *et al*, 2006), although the *in vivo* effect has not been made known. To estimate the tumour state after treatment with TβR-I inhibitor is important to determine an administration schedule for TβR-I inhibitor-combined therapy. However, it is difficult to rationally determine whether tumour blood vessels are amenable to nanocarrier-mediated therapy in an individualised manner.

Dynamic contrast-enhanced magnetic resonance imaging (DCE-MRI) is one of the evaluation methods of anti-angiogenic agents, such as anti-VEGF antibody and tyrosine kinase inhibitor, clinically (Morgan *et al*, 2003; O'Connor *et al*, 2007) and preclinically (Marzola *et al*, 2004; Nakamura *et al*, 2006; Bradley *et al*, 2009), by calculating pharmacokinetic parameters, including fractional plasma volume (v_p) and the volume transfer constant (K^{trans}) from the enhancement of tumour signal intensity by gadolinium (Gd) contrast agent (Tozer, 2003; Kiessling *et al*, 2007). To my knowledge, however, there are no reports to evaluate TβR-I inhibitor by DCE-MRI. In clinical studies, small molecular weight contrast agents, Gd chelates, have been used. K^{trans}, the Gd exchange constant between blood and tumour interstitial tissue, depends on the balance between permeability and blood flow. Therefore, the K^{trans} parameter depends on the size of the contrast

*Correspondence: Dr Y Maitani; E-mail: yoshie@hoshi.ac.jp
Received 8 July 2009; revised 2 September 2009; accepted 17 September 2009; published online 3 November 2009

agent. The choice of the optimal contrast agent is considered to be essential for a successful characterisation of tumour angiogenesis. As macromolecule contrast media show lower permeability than Gd cheleates, it is useful for permeability change monitoring in tumour vasculature (Daldrup-Link *et al*, 2004; Turetschek *et al*, 2004); Liposomes are self-closed colloidal particles in which bilayer membranes composed from self-aggregated lipid molecules encapsulate a fraction of the medium. Liposomes have been used as drug carriers for anticancer drugs such as Doxil. For this reason, liposomal Gd has a substantial potential to detect permeability-limited conditions. There are still no reports on the use of liposomes as a DCE-MRI contrast agent. Furthermore, liposomal contrast agents to evaluate nanocarrier behaviour in tumour directly will be a hopeful method of examination for combination therapy.

Thus, the purpose of this study was to evaluate changes in tumour vasculature as parameters using DCE-MRI to monitor responses in mice following A-83-01 administration. In addition to DCE-MRI, diffusion-weighted imaging was used to estimate *the apparent diffusion coefficient* of tissue water (Koh and Padhani, 2006; Patterson *et al*, 2008). TβR-I inhibitor activity was also evaluated in representative experiments through tumour vascularity, the proportion of endothelial cells associated with pericytes, and microvessel density from histological slices.

MATERIALS AND METHODS

Animals

All animal experiments were carried out in accordance with the guidelines of the Guiding Principles for the Care and Use of Laboratory Animals of Hoshi University. Colon 26 cells (1×10^6) were inoculated subcutaneously into the right back at the side of the heart in CDF1 female mice (6-weeks old, Sankyo Labo Service, Tokyo, Japan). When the tumour size reached approximately 100 mm^3, A-83-01 (Sigma Chemical, St. Louis, MO, USA) (Supplementary Figure S1A) dissolved in DMSO/saline = 3 out of 2 (v/v) was injected intraperitoneally. The tail vein was catheterised post-injection of contrast agent during the DCE-MRI experiment. Mice were anaesthetised with 1.5% isoflurane (Abbott Japan, Tokyo, Japan) throughout the MRI experiment during their insertion into a 9.4T vertical type MRI (Varian, Palo Alto, CA, USA). For a single treatment of A-83-01, mice (N = 4) were injected with A-83-01 at a dose of 1 mg kg^{-1} at '0 h' (Supplementary Figure S1B). In this experiment, 0 h was the time of the first A-83-01 intraperitoneal injection and the number of hours represents time after the first injection of A-83-01. For repeated treatment, mice (N = 4) were injected with A-83-01 at 0 and 21 h at the same dose as for the single treatment.

Preparation of liposomal Gd-DTPA

For the preparation of liposomal Gd-DTPA (Gd-L), mixture of egg phosphatidylcholine (Q.P. Company, Tokyo, Japan), cholesterol (Wako Pure Chemical Industries, Osaka, Japan), and polyethyleneglycol 2000-distearoyl phosphatidylethanolamine (NOF, Tokyo, Japan) in a molar ratio of 5 : 2 : 0.35 was dissolved in ethanol at 60°C, hydrated with Gd-DTPA (Magnevist, Bayer-Schering Pharma AG, Berlin, Germany), stirred, and evaporated under a vacuum to remove ethanol. This mixture was exposed to ultrasound until the particle diameter was about 120 nm, followed by exhausted dialysis against phosphate buffered saline (pH 7.4) solution. The particle size of the liposomes was determined at 25°C using an ELS-Z2 instrument (Otsuka Electronics, Tokyo, Japan). The Gd concentration was determined using *inductively coupled plasma* with an SPS7800 apparatus (SII NanoTechnology, Tokyo, Japan). T^1 relaxation times of Gd-L and Gd-DTPA were measured over the concentration range of 0–0.25 mM Gd at 9.4 T_1 at room temperature. Relaxivity (R^1) was then determined from the slope of the linear regression fits of $1/T_1$ *vs* the Gd concentration: $1/T_1 = R_1 \times [Gd] + 1/T_{10}$, where T_{10} represents T_1 of 0 mM Gd solution. R_1 of Gd-L was 4.48 $mM^{-1}s^{-1}$, which was similar to that of Gd-DTPA (4.39 $mM^{-1}s^{-1}$).

MRI

Apparent diffusion coefficient was estimated and mapped from *diffusion-weighted imaging* using the following parameters: repetition time (TR) = 2000 ms, echo time (TE) = 45 ms, slice thickness 3 mm, 64 × 64 data matrix, axial orientation, and field-of-view of 3 × 3 cm^2. Three slices through the centre of the tumour were acquired. Diffusion gradients equivalent to b-values of 0, 200, 400, and 800 s mm^{-2} were employed using gradient pulse widths of $\delta = 7$ ms and $\Delta = 20$ ms.

Dynamic contrast-enhanced magnetic resonance imaging was carried out with Gd-DTPA and Gd-L before ('pre') and after treatment in each animal. With the use of Gd Gd-L, injected lipids containing Gd-L were retained in the tumour; therefore, different mice were used to compare pretreatment with treatment of A-83-01. Before DCE-MRI high spatial resolution, two-dimensional T_2-weighted spin–echo axial images were acquired to detect the tumour position. Pre-contrast tumour T_1 was determined using an inversion recovery-prepared spoiled gradient-recalled echo (SPGR) sequence. The inversion-recovery was carried out using a 180° hard RF pulse followed by a gradient crusher pulse. Inversion times were 0.2, 0.4, 0.8, 1.4, 2, and 3 s. The other MRI parameters were: TE = 3 ms, field-of-view = 3 × 3 cm^2, slice thickness = 4 mm, and matrix size = 64 × 64. Both RF and gradient spoilers were applied. In DCE-MRI acquisition, it was applied repeatedly to acquire the axial slice SPGR images through the tumour and left ventricle with a second temporal resolution over 6 min: TR = 7.8125 ms, TE = 2.06 ms, matrix resolution = 64 × 64, field-of-view = 3 × 3 cm^2, slice thickness = 4 mm, flip angle = 30°, number of slices = 1, and two signal averages. Approximately 20 s of baseline DCE-MRI images were acquired. Gd-DTPA or Gd-L was administered at 20 μl g^{-1} (0.1 mmol Gd kg^{-1}) as a bolus with heparinized saline (total volume ~0.4 ml) via manual injection over 2–3 s.

Quantitative evaluation of MRI

Tumour regions-of-interest (ROI) covering the whole tumour was segmented on the T_2-weighted axial images, using ImageJ software (NIH, Bethesda, MD, USA), and the tumour ROI was transferred to the *apparent diffusion coefficient* map calculated from *diffusion-weighted imagings*.

A T_1 map of tumour was prepared by the imaging of the inversion-recovery method to quantitate tumour Gd concentrations. The concentration of Gd at each imaging time point in each voxel was estimated using the formula Bradley *et al* (2009) used. T_1 in blood plasma at 9.4 T was 2.2 s, as reported previously (Tsekos *et al*, 1998) and T_1 in tumour was from the T_1 map. $1/T_1$ (t) was calculated for every time point for the blood and tumour Gd concentrations . The initial area under the Gd concentration–time curve over 60 s ($IAUGC_{60}$) was calculated. The tumour haemodynamic parameters K^{trans} and v_p were calculated using a two-compartment model (Ewing *et al*, 2003). The plasma concentration over time was calculated from the left ventricle data, which were averaged for all mice in the Gd-DTPA and Gd-L groups for this value.

Histological and immunohistochemical analysis

For the histological assessment of A-83-01 effects on tumour vasculature, tumour sections were observed at 24 h after repeated injection of A-83-01. Each of four tumours from A-83-01 treated

and untreated mice was resected and fixed with 10% formalin. Paraffin-embedded samples were sliced into 3 μM sections for *hematoxylin and eosin* staining and immunostaining. Antibodies against α-smooth muscle actin (SMA) (DAKO, Glostrup, Denmark) were used to identify the pericyte and anti-CD31 (Abcam, MA, USA, USA), endothelial cell marker and anti-Ki67 (Labvision, Fremont, CA, USA) antibodies to recognise the growth state cells (G1, S, and M phase). Vascular areas within the tumours were measured as the index of tumour vascularity by stained with anti-CD31. Five fields of tumour sections were analysed at low magnification using a computerised image analyser (Image-Pro Plus, Media Cybernetics, MA, USA). The ratio of vessel area against tumour area without necrosis was calculated.

Statistical analysis

Values were expressed as the mean ± s.d. A two-tailed Student's *t*-test was used comparison between the pre- and post-treatment groups. ANOVA analysis, followed by Dunnett's test, was used for multi-group comparisons. Pearson's correlation coefficients were used for determination between a significant positive and negative relationship. Correlations between 0.4 and 0.6 were considered moderate, whereas correlations from 0.7 to 1.0 were considered strong. Significant differences were accepted when the *P*-value was below 0.05.

RESULTS

Figure 1A shows change of the Gd concentrations in DCE-MRI acquisition using Gd-DTPA at pretreatment, at 3-h, and 24-h post-injection of A-83-01. A progressive accumulation of Gd in the tumour was observed during the first 60 s followed by a plateau phase. The group treated with a single injection of A-83-01 showed the highest accumulation at 3 h post-injection of A-83-01 (1.7-fold the $IAUGC_{60}$, Figure 1B) associated with a larger s.d., and a similar level to those with pretreatment at 24 h (0.9-fold the $IAUGC_{60}$). At 24 h after repeated injection, the tumour accumulation increased a similar level to that at 3 h after the single injection (1.8-fold the $IAUGC_{60}$). Next, we observed changes of the tumour vasculature repeat-treated by A-83-01 using Gd-L. The Gd concentration in DCE-MRI acquisition of untreated mice was very low (Figure 1C). The Gd concentration with Gd-L in repeat-treated mice increased during the first 200 s, and reached the same plateau value as with that of the Gd-DTPA repeat-treated mice. Eventually the repeated A-83-01 treatment increased 3.8-fold the $IAUGC_{60}$ of Gd-L (Figure 1D), indicating a dramatic improvement in liposomal contrast agent delivery to the tumour.

From the data obtained above, v_p and K^{trans} values were calculated (Figure 2). With Gd-DTPA at 3 h after the single treatment, v_p and K^{trans} were high values accompanied with great variability, whereas at 24 h, v_p and K^{trans} were similar to those of the respective pretreatment values, suggesting that A-83-01 induced a transient change in the vasculature at around 3 h. On the other hand, at 24 h after repeated treatment, all mice showed increased v_p and K^{trans} with Gd-DTPA ($P<0.05$) and Gd-L. At 3 h after the first treatment, v_p and K^{trans} did not show significantly elevated values with Gd-DTPA, therefore, it can be concluded that the repeated administration schedule changed the tumour state positively for better liposomal contrast-agent distribution. The most characteristic point of the v_p and K^{trans} changes was the large dispersion of v_p and K^{trans} values after repeated A-83-01 treatments with the use of Gd-L. The diversity of local permeability of treated tumours may lead to large

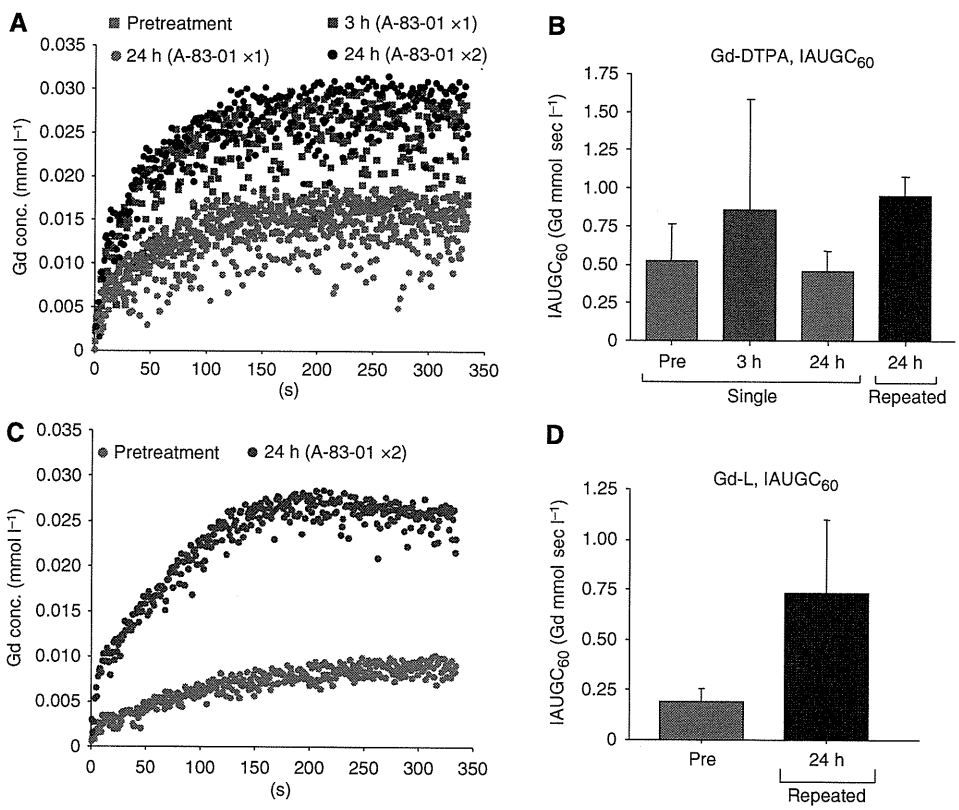

Figure 1 Mean gadolinium (Gd) uptake curves from regions-of-interest (ROI) over the whole tumour before (pre) and at different time points after (post) intraperitoneal A-83-01 injection with Gd-DTPA (**A**) and Gd-L (**C**), and $IAUGC60_{0-60}$ with Gd-DTPA (**B**) and Gd-L (**D**). Data points (**B**, **D**) indicate mean ± s.d. (N = 3–6).

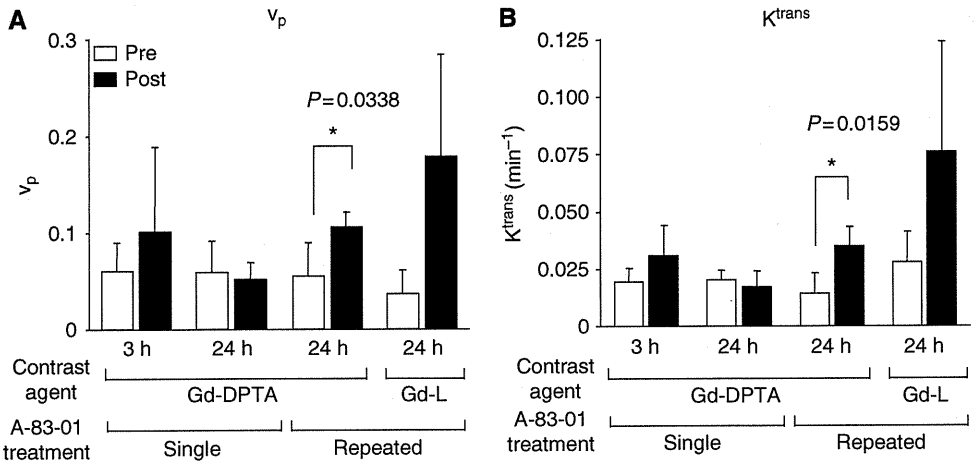

Figure 2 Values of fractional plasma volume (v_p) (**A**) and volume transfer constant (K^{trans}) (**B**) in the tumour before (pre) and at 3 h and 24 h after (post) single or repeated A-83-01 injections using gadolinium (Gd)-DTPA and Gd-L as a contrast agent. Each column represents the mean ± SD (N = 3 to 6).

dispersion of Gd-L. The mouse tumour core showed an increase in the Gd concentration, as shown in Figure 1C, whereas the tumour rim showed a high peak concentration at about 1 min post-injection of Gd-L that then decayed (data not shown). In contrast, Gd-DTPA increased tumour Gd concentration homogeneously. This finding suggests that Gd-L could detect small changes in tumour micro-environments and brought about a big dispersion of v_p and K^{trans} values among treated mice.

Figure 3 shows histological observations of the tumours with or without the repeated A-83-01 treatment. Two distinct changes were observed, although there was no difference in tumour cell shape or necrosis. The first was intra-tumoural bleeding, which was exclusively configured at the periphery of the A-83-01-treated tumours with 200–300 μm width and 100 μm depth (Figure 3A). The bleeding lesions were not accompanied with tissue oedema, suggesting minute rupture of tumour vessels. This means that hyper-permeability had not occurred. The localised bleeding state may correspond to the accumulation site of Gd-L. The second observation was morphological changes of the tumour vasculature. Abnormal blood vessels with irregular dilation were seen in the untreated tumours, whereas the vasculature in A-83-01-treated mice was smaller, and its shape was more round, suggesting the vascular normalisation (Figure 3A). Tumour vascularity, the percentage of vascular area (1.2%) in the treated tumours (post) was not significantly lower than in the untreated tumours (pre, 2.9%, $P > 0.05$), as the change was very diverse within a tumour (Figure 3D). The abnormal tumour vessels were not accompanied with pericytes, which were identified because of SMA reactivity (Figure 3B). It is interesting to note that the normalised vessels in tumours treated with A-83-01 were surrounded by pericytes (Figure 3B). The Ki67 index (58.5%) was significantly higher in the perivascular region of the A-83-01-treated tumours compared with the untreated tumours (41.4%, $P < 0.05$) (Figure 3C, E). These findings suggested that the repeated A-83-01 treatment allowed the recovery of blood flow during 24 h.

In the evaluation of *apparent diffusion coefficient* value, single-treated groups at 3 and 24 h did not show a difference compared with the pretreatment, but the repeat-treated group at 24 h showed a significant difference ($P < 0.01$, Figure 4). Alteration of extra- and intracellular fluid volume balance in repeat-administrated protocol may occur in the tumour because the diffusion rate of intracellular water is 1 order of magnitude smaller than that of the extracellular water (Van Zijl *et al*, 1991; Gass *et al*, 2001).

Next, the relation of DCE-MRI parameters with Gd-DTPA to tumour *apparent diffusion coefficient* was investigated (Figure 5). There was a moderately negative correlation between *the IAUGC*$_{60}$ (Figure 5A), K^{trans} (Figure 5B), v_p, *and apparent diffusion coefficient* (Figure 5C). This suggests that these parameters may be of value in the assessment of tumour behaviour.

DISCUSSION

In this study, effects of a TβR-I inhibitor was firstly evaluated by means of DCE-MRI with Gd-DTPA and Gd-L in mice bearing colon 26 tumours. The effect of A-83-01 exhibited high IAUGC$_{60}$, v_p, and K^{trans} values at 24 h after repeated treatment.

An increase in K^{trans} by the use of Gd-L could conceivably increase the permeability and surface area of the capillary endothelium. The K^{trans} value estimated with Gd-L ($K^{trans} = 0.076 \pm 0.048$ min^{-1}) after the repeated A-83-01 treatment was higher to that with Gd-DTPA ($K^{trans} = 0.035 \pm 0.009$ min^{-1}) (Figure 2B). Liposomal contrast agents are promising for characterising the tumour vascularity and the angiogenesis status through DCE-MRI method.

Anti-angiogenic agents such as anti-VEGF antibody and tyrosine kinase inhibitor were reported that decrease both K^{trans} and IAUGC (O'Connor *et al*, 2007; Bradley *et al*, 2008; Bradley *et al*, 2009), and the decrease in K^{trans} in solid tumours is concerned with the anti-tumour effect (Morgan *et al*, 2003; Marzola *et al*, 2004; Nakamura *et al*, 2006; Flaherty *et al*, 2008). In this study, K^{trans}, IAUGC$_{60}$, and v_p were increased significantly 24 h after the A-83-01 treatment. This increase may be explained by different treatment protocols, different tumour models, and the different signal inhibition between anti-angiogenic agent such as kinase inhibitor and TβR-I inhibitor. Similar to A-83-01-treated colon 26 solid tumours, LY364947-treated M109 solid tumours increased IAUGC$_{60}$ at 3 h and recovered fully by 24 h post-injection (Supplementary Figure S2).

It was reported that in a limited situation, anti-angiogenic agents work to deliver more drugs into tumours through the induction of vascular normalisation (Jain, 2001). Untreated colon 26 tumours showed low permeability, in spite of the absence of pericytes or the leaky vessel state (Figure 2B, 3B). The increased K^{trans} and IAUGC$_{60}$ values were related to the increased number of growth state cells around the tumour vessel, and were correlated to the decreased *apparent diffusion coefficient value*. Because of no significant difference in tumour cell shape after treatment (Figure 3A), intra-cellular volume did not change. Decreased *apparent diffusion coefficient*, therefore, reflected a decrease in

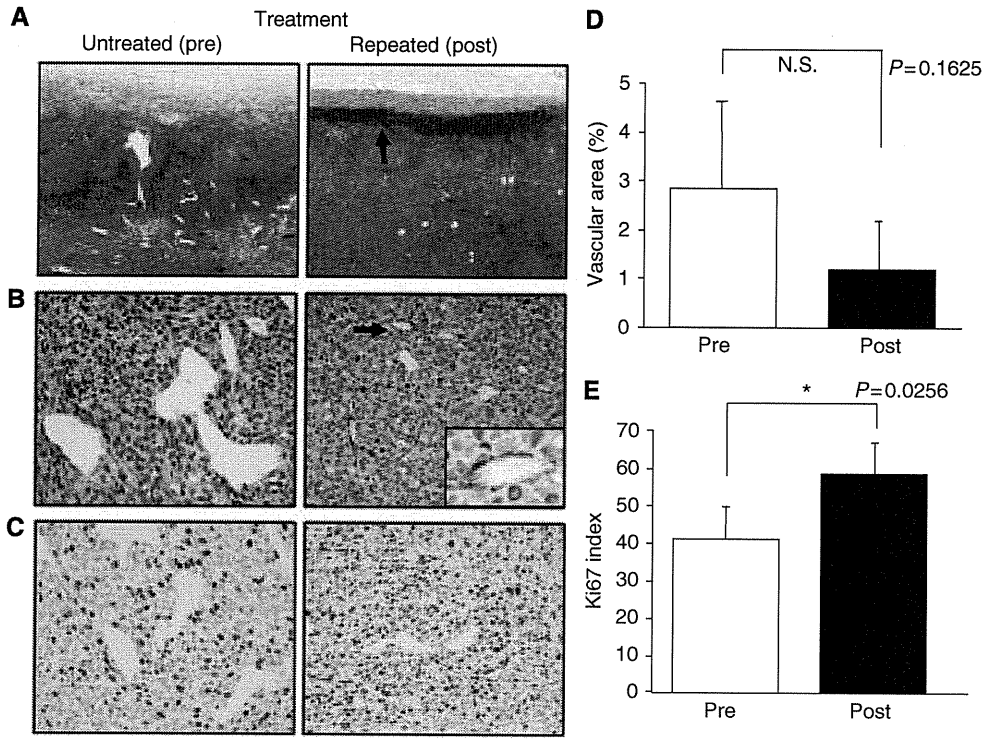

Figure 3 Histological analysis of tumours in untreated (pre) and treated (post) mice 24 h after repeated A-83-01 treatment. (**A**) *Hematoxylin and eosin* staining (× 40). Arrow indicates that zonal bleeding was observed at the periphery of the tumour with A-83-01 treatment. (**B**) Immunostaining with anti-smooth muscle actin (SMA) antibody (× 200 and inset, × 400). Irregularly dilated tumour vessels in untreated mice are not associated with pericytes, whereas the normalized vessels after A-83-01 treatment are surrounded by SMA-positive pericytes (arrow). (**C**) Immunostaining with Ki67. Ki67-positive proliferating tumour cells in the perivascular region are more prominent in the A-83-01 treated tumour than the untreated tumour (× 200). (**D**) Mean percentage of the vascular areas within the tumours as the index of tumour vascularity. (**E**) Ki67 index in perivascular regions of (**C**). Proliferating tumour cells were increased significantly in A-83-01 treated tumours compared with untreated tumours ($P<0.05$). Each column represents the mean ± s.d. (N = 5).

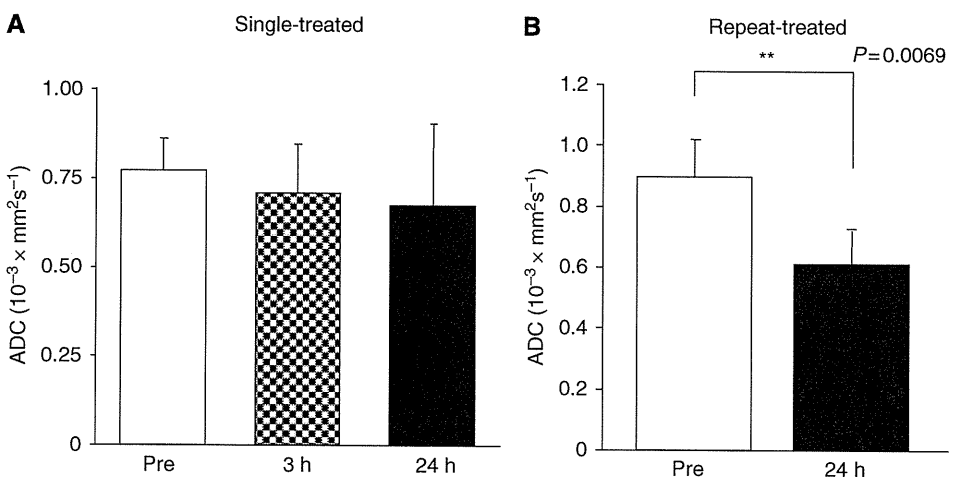

Figure 4 *Apparent diffusion coefficient* of the tumours before (pre) and at different time points after (post) single (**A**) and repeated (**B**) intraperitoneal A-83-01 injection. Repeat-treated tumours showed significant decreases in *apparent diffusion coefficient* compared with pretreatment. Each column represents the mean ± s.d. (N = 4).

extra-cellular fluid, suggesting that the recovery of delivery may be related to vessel normalisation.

Furthermore, similar to negative correlation between tumour interstitial fluid pressure and permeability of tumour (Haider *et al*, 2007), IAUGC, K^{trans}, and v_p showed a moderate negative correlation to *apparent diffusion coefficient*, suggesting that these parameters may be providing similar information. As *apparent diffusion coefficient* is acquired in clinic widely to detect and diagnose a tumour, it could apply conveniently to examine the permeability of tumour in patients.

Although there is room for improvement, DCE-MRI using liposomal contrast agents such as Gd-L could be an important method to anticipate the extravasation of the liposomal anti-cancer drug during TβR-I inhibitor-combined therapy.

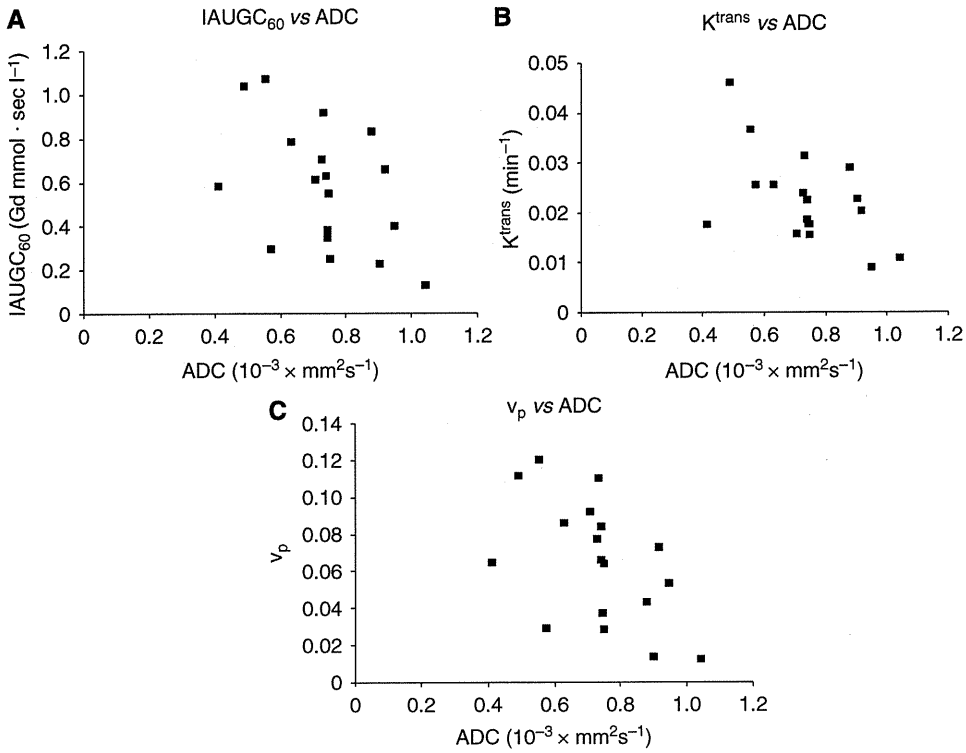

Figure 5 $IAUGC_{60}$, transfer constant volume transfer constant (K^{trans}), and fractional plasma volume (v_p) with gadolinium (Gd)-DTPA *vs* tumour *apparent diffusion coefficient* (*ADC*). There was a moderately negative correlation between the $IAUGC_{60}$ and ADC ($r=-0.4774$, $P=0.0451$, $N=18$) (**A**), between K^{trans} and ADC ($r=-0.5333$, $P=0.0227$, $N=18$) (**B**), and between v_p and ADC ($r=-0.5253$, $P=0.0252$, $N=18$) (**C**).

In summary, we found that DCE-MRI parameters, K^{trans}, $IAUGC_{60}$, and v_p were positively related to tumour vasculature by the treatment of A-83-01. Thus, TβR-I inhibitor has the potential to enhance the delivery of liposomal anti-cancer drugs and contrast agents. DCE-MRI forms a capable tool to determine the administration schedule of combination therapy with TβR-I inhibitor by K^{trans} and v_p quantitation.

ACKNOWLEDGEMENTS

This work was supported in part by a grant for research on Regulatory Science of Pharmaceuticals and Medical Devices from the Ministry of Health, Labor and Welfare of Japan and by the Open Research Center Project. Ms Y Taniguchi is acknowledged for providing many helpful comments, and Mr S Kawagoe and Mr T Nakamura for assistance.

REFERENCES

Bradley DP, Tessier JJ, Lacey T, Scott M, Jurgensmeier JM, Odedra R, Mills J, Kilburn L, Wedge SR (2009) Examining the acute effects of cediranib (RECENTIN, AZD2171) treatment in tumor models: a dynamic contrast-enhanced MRI study using gadopentate. *Magn Reson Imaging* **27:** 377–384

Bradley DP, Tessier JL, Checkley D, Kuribayashi H, Waterton JC, Kendrew J, Wedge SR (2008) Effects of AZD2171 and vandetanib (ZD6474, Zactima) on haemodynamic variables in an SW620 human colon tumour model: an investigation using dynamic contrast-enhanced MRI and the rapid clearance blood pool contrast agent, P792 (gadomelitol). *NMR Biomed* **21:** 42–52

Daldrup-Link HE, Okuhata Y, Wolfe A, Srivastav S, Oie S, Ferrara N, Cohen RL, Shames DM, Brasch RC (2004) Decrease in tumor apparent permeability-surface area product to a MRI macromolecular contrast medium following angiogenesis inhibition with correlations to cytotoxic drug accumulation. *Microcirculation* **11:** 387–396

Ewing JR, Knight RA, Nagaraja TN, Yee JS, Nagesh V, Whitton PA, Li L, Fenstermacher JD (2003) Patlak plots of Gd-DTPA MRI data yield blood-brain transfer constants concordant with those of 14C-sucrose in areas of blood-brain opening. *Magn Reson Med* **50:** 283–292

Flaherty KT, Rosen MA, Heitjan DF, Gallagher ML, Schwartz B, Schnall MD, O'Dwyer PJ (2008) Pilot study of DCE-MRI to predict progression-free survival with sorafenib therapy in renal cell carcinoma. *Cancer Biol Ther* **7:** 496–501

Gass A, Niendorf T, Hirsch JG (2001) Acute and chronic changes of the apparent diffusion coefficient in neurological disorders–biophysical mechanisms and possible underlying histopathology. *J Neurol Sci* **186:** S15–S23

Haider MA, Sitartchouk I, Roberts TP, Fyles A, Hashmi AT, Milosevic M (2007) Correlations between dynamic contrast-enhanced magnetic resonance imaging-derived measures of tumor microvasculature and interstitial fluid pressure in patients with cervical cancer. *J Magn Reson Imaging* **25:** 153–159

Jain RK (2001) Normalizing tumor vasculature with anti-angiogenic therapy: a new paradigm for combination therapy. *Nat Med* **7:** 987–989

Jakowlew SB (2006) Transforming growth factor-beta in cancer and metastasis. *Cancer Metastasis Rev* **25:** 435–457

Kano MR, Bae Y, Iwata C, Morishita Y, Yashiro M, Oka M, Fujii T, Komuro A, Kiyono K, Kaminishi M, Hirakawa K, Ouchi Y, Nishiyama N, Kataoka K, Miyazono K (2007) Improvement of cancer-targeting therapy, using nanocarriers for intractable solid tumors by inhibition of TGF-beta signaling. *Proc Natl Acad Sci USA* **104:** 3460–3465

Kiessling F, Morgenstern B, Zhang C (2007) Contrast agents and applications to assess tumor angiogenesis *in vivo* by magnetic resonance imaging. *Curr Med Chem* **14:** 77–91

Koh DM, Padhani AR (2006) Diffusion-weighted MRI: a new functional clinical technique for tumour imaging. *Br J Radiol* **79:** 633–635

Li HY, Wang Y, Heap CR, King CH, Mundla SR, Voss M, Clawson DK, Yan L, Campbell RM, Anderson BD, Wagner JR, Britt K, Lu KX, McMillen WT, Yingling JM (2006) Dihydropyrrolopyrazole transforming growth factor-beta type I receptor kinase domain inhibitors: a novel benzimidazole series with selectivity versus transforming growth factor-beta type II receptor kinase and mixed lineage kinase-7. *J Med Chem* **49:** 2138–2142

Marzola P, Degrassi A, Calderan L, Farace P, Crescimanno C, Nicolato E, Giusti A, Pesenti E, Terron A, Sbarbati A, Abrams T, Murray L, Osculati F (2004) In vivo assessment of antiangiogenic activity of SU6668 in an experimental colon carcinoma model. *Clin Cancer Res* **10:** 739–750

Matsumura Y, Maeda H (1986) A new concept for macromolecular therapeutics in cancer chemotherapy: mechanism of tumoritropic accumulation of proteins and the antitumor agent smancs. *Cancer Res* **46:** 6387–6392

Morgan B, Thomas AL, Drevs J, Hennig J, Buchert M, Jivan A, Horsfield MA, Mross K, Ball HA, Lee L, Mietlowski W, Fuxuis S, Unger C, O'Byrne K, Henry A, Cherryman GR, Laurent D, Dugan M, Marme D, Steward WP (2003) Dynamic contrast-enhanced magnetic resonance imaging as a biomarker for the pharmacological response of PTK787/ZK 222584, an inhibitor of the vascular endothelial growth factor receptor tyrosine kinases, in patients with advanced colorectal cancer and liver metastases: results from two phase I studies. *J Clin Oncol* **21:** 3955–3964

Nakamura K, Taguchi E, Miura T, Yamamoto A, Takahashi K, Bichat F, Guilbaud N, Hasegawa K, Kubo K, Fujiwara Y, Suzuki R, Kubo K, Shibuya M, Isae T (2006) KRN951, a highly potent inhibitor of vascular endothelial growth factor receptor tyrosine kinases, has antitumor activities and affects functional vascular properties. *Cancer Res* **66:** 9134–9142

O'Connor JP, Jackson A, Parker GJ, Jayson GC (2007) DCE-MRI biomarkers in the clinical evaluation of antiangiogenic and vascular disrupting agents. *Br J Cancer* **96:** 189–195

Patterson DM, Padhani AR, Collins DJ (2008) Technology insight: water diffusion MRI–a potential new biomarker of response to cancer therapy. *Nat Clin Pract Oncol* **5:** 220–233

Tojo M, Hamashima Y, Hanyu A, Kajimoto T, Saitoh M, Miyazono K, Node M, Imamura T (2005) The ALK-5 inhibitor A-83-01 inhibits Smad signaling and epithelial-to-mesenchymal transition by transforming growth factor-beta. *Cancer Sci* **96:** 791–800

Tozer GM (2003) Measuring tumour vascular response to antivascular and antiangiogenic drugs. *Br J Radiol* **76:** S23–S35

Tsekos NV, Zhang F, Merkle H, Nagayama M, Iadecola C, Kim SG (1998) Quantitative measurements of cerebral blood flow in rats using the FAIR technique: correlation with previous iodoantipyrine autoradiographic studies. *Magn Reson Med* **39:** 564–573

Tsuchida K, Sunada Y, Noji S, Murakami T, Uezumi A, Nakatani M (2006) Inhibitors of the TGF-beta superfamily and their clinical applications. *Mini Rev Med Chem* **6:** 1255–1261

Turetschek K, Preda A, Novikov V, Brasch RC, Weinmann HJ, Wunderbaldinger P, Roberts TP (2004) Tumor microvascular changes in antiangiogenic treatment: assessment by magnetic resonance contrast media of different molecular weights. *J Magn Reson Imaging* **20:** 138–144

Van Zijl PC, Moonen CT, Faustino P, Pekar J, Kaplan O, Cohen JS (1991) Complete separation of intracellular and extracellular information in NMR spectra of perfused cells by diffusion-weighted spectroscopy. *Proc Natl Acad Sci USA* **88:** 3228–3232

＊研究論文＊

Iterative Region-of-Interest Reconstruction From Truncated CT Projection Data Under Blind Object Support

Essam A. RASHED[*1], Hiroyuki KUDO[*1], Frédéric NOO[*2]

Abstract

We have investigated image reconstruction from truncated projection data in computed tomography. Region-of-interest (ROI) imaging techniques, which are practically implemented by limiting X-ray exposure to the target region of the object, provide so-called truncated projection data. This limitation in the projection data converts the image reconstruction problem to an undetermined problem in which extra effort is needed to achieve accurate ROI reconstruction. Recently developed theories based on differentiated backprojection (DBP) suggest the possibility of achieving accurate ROI imaging in some clinical imaging scenarios. An essential requirement for achieving exact ROI reconstruction is prior knowledge of the object support (OS). However, the exact OS is not always available in many imaging applications. In this paper, first, we investigate how the image artifacts depend on the accuracy of the *a priori* known OS, and second, we propose an EM-based iterative reconstruction algorithm to reduce the ROI artifacts when the OS is unknown. The image reconstruction cost function is modified to include a thresholding function in the form of ℓ_0 norm, and thanks to this modification, the OS is automatically detected by the thresholding function and the ROI artifacts are reduced. The experimental results, including numerical simulations and real data with different ROI and object configurations, indicate that a significant reduction in ROI artifacts can be achieved by using the proposed algorithm.

Key words: Tomography, Image reconstruction, ROI imaging, Truncated projection data, Object support

Med Imag Tech **27**(5): 321-331, 2009

1. Introduction

Computed Tomography (CT) has become the most popular medical imaging modality to diagnose various diseases. The widespread use of CT increased the radiation dose in the population as CT involves much higher dose over the traditional plain-film radiography [1]. The interest was recently focused on developing reconstruction algorithms from low dose CT projection data to reduce the radiation dose. The dose reduction is challenging as the decreasing of the x-ray beam intensity increases the statistical noise in the reconstructed images. One possible approach to achieve the dose reduction is the Region-of-Interest (ROI) CT imaging by focusing the radiation only to the organ of interest, which reduces unnecessary radiation to the remaining portion of the patient. This imaging setup directly leads to data truncation problem in which left and/or right portions of the projection data are missing for all the view angles. **Fig. 1** illustrates CT imaging setups for the full scan and the ROI scan. The topic of ROI imaging has been studied for a long time (e.g. [2 ~ 5]) and, based on the concept of analytical reconstruction, it had been believed that ROI reconstruction, even for a small ROI, requires all projection rays passing through the whole object and any truncation leads to losing the solution exactness. However, the recently developed theories based on

[*1] Department of Computer Science, Graduate School of Systems and Information Engineering, University of Tsukuba [Tennoudai 1-1-1, Tsukuba 305-8573, Japan]
[*2] Department of Radiology, University of Utah, UT, USA
e-mail: essam@imagelab.cs.tsukuba.ac.jp
receive: April 20, 2009
accept: october 8, 2009

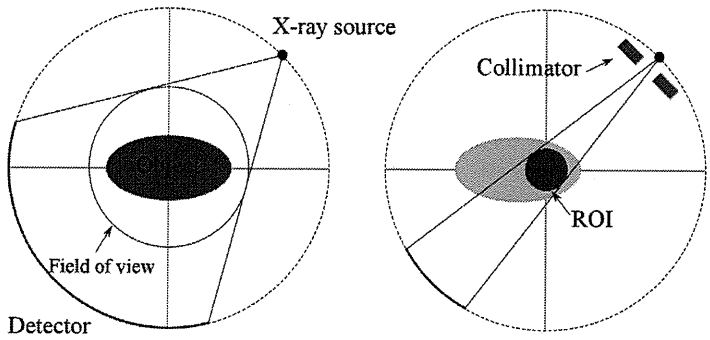

Fig. 1 CT imaging configurations for whole object imaging (left) and ROI imaging (right).

the concept of Differentiated Backprojection (DBP) [6] and Backprojection-Filtration (BPF) [7] succeeded in reducing the required set of projection rays for theoretically exact and stable ROI reconstruction. It became clear that the position of the ROI is an important factor to determine the possibility of accurate ROI reconstruction. Defrise et al. [8] provided a sufficient condition for accurate ROI reconstruction with truncated projection data. The exact reconstruction requires that the ROI contains a small limited region inside [9, 10] or outside the object with known intensity values. Practically, the availability of accurate prior information inside the object is difficult, however selecting this region as a portion of the background is more feasible as the attenuation value of air is known to be almost zero. Enforcing this *a priori* information of the background region is usually done using the Object Support (OS) constraint during image reconstruction. The OS is the region where the object is certainly inside. In real applications, however, the *a priori* knowledge of the OS is not always available or requires extra efforts to be estimated accurately. Alternatively, OS is selected a slightly larger than the true object to ensure that the object is located completely inside. Through numerical studies, it is known that the lack of exact OS produces DC-shift and low-frequency artifacts in the reconstructed images [11, 12].

The aim of this paper is two-fold. The first aim is to evaluate the relation between the accuracy of prior knowledge of OS constraint and the quality of image reconstructed from truncated projection data. The second aim is to propose an iterative ROI reconstruction algorithm from truncated projection data when the OS is unknown or technically unavailable. Throughout this paper, we consider the truncated projection data such that only the projection rays passing through the ROI are measured. These settings are suitable to achieve a reduction in the radiation exposure outside the ROI. In the proposed algorithm, the cost function is modified to include a thresholding function in the form of ℓ_0 norm distance. The OS is then automatically estimated by the thresholding function and iteratively converges towards the exact one. In section 2, we explain necessary basic concepts and the proposed iterative reconstruction algorithm. In section 3, we present numerical results of simulation studies and real data. In section 4, we conclude the paper.

2. Methodology

1) Object support constraint

We assume that the projection data is truncated such that it includes only the projection rays corresponding to all lines passing through a limited ROI Ω. We represent the OS (the *a priori* known region where the object is certainly inside) by μ. Then, the exact reconstruction of Ω is possible if there exists a set of pixels x_j such that $x_j \in \Omega$ and $x_j \notin \mu$ [8]. In other words, ROI should be defined such that it includes a limited region outside the OS where the intensity value is *a priori* known to be zero. Two different imaging configurations are shown in **Fig. 2** that illustrates Defrise's condition. In the setup of (a), the exact reconstruction is possible as the ROI is selected such that it contains a small region outside the OS μ (hatched area), while the exact reconstruction is theoretically not possible in the setup of (b) as it corresponds to the so-called *interior problem* [13]. The challenging of this theory is that, when the accuracy of OS is worse, the observed ROI should be selected to cover a larger region of the scanned

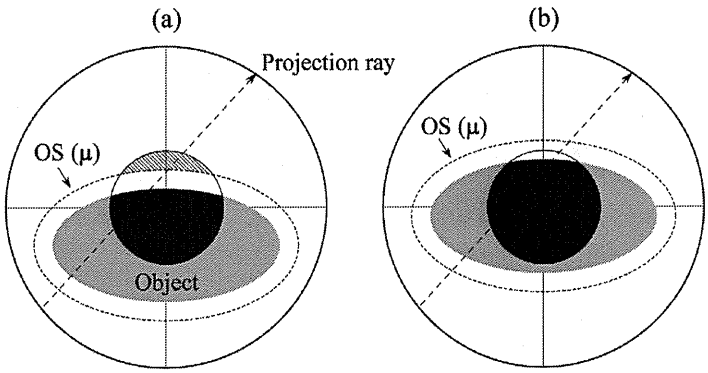

Fig. 2 Two different ROI imaging configurations, (a) ROI contains a region (shaded) outside the OS (Defrise's condition is satisfied and the solution exactness is assured) and (b) ROI is contained completely inside the OS (interior problem and the solution is not unique).

object and a larger area outside the object. A typical clinical application that demonstrates these imaging configurations is the cardiac ROI imaging. To obtain a theoretically accurate reconstruction, the ROI should be selected carefully such that it includes a region where the intensity value is *a priori* known to be zero. Considering the fact that it is difficult to determine the exact contours for different patients (exact OS) in prior to imaging, the ROI should be selected large enough to include the target object (heart) and the region outside the OS similarly to the setup of **Fig. 2**(a). The aim of this work is to estimate the exact OS during image reconstruction. This will allow us to reduce the size of ROI leading to dose reduction and other benefits. Finally, we remark that analytical solution have not been found yet for this truncation problem so that using iterative algorithms is an only way to perform image reconstruction in this problem [8~10].

2) Iterative algorithms with zero-pixels identification

To estimate the OS, for example, iterative algorithms which alternate image reconstruction and zero-pixels identification (by thresholding or image segmentation) can be considered. However, such brute-force algorithms cannot be implemented efficiently and their convergences are not guaranteed in general. In this paper, we introduce a more sophisticated class of iterative algorithms based on the relatively new concept of so-called sparse signal recovery or compressed sensing[14]. The main idea is to include a distance function consisting of ℓ_1 / ℓ_0 norm of reconstructed images into the cost function for image reconstruction. Then, this additional ℓ_1 / ℓ_0 norm term works as a thresholding operation applied after each iteration step, which replaces small pixels values to zeros (i.e. identifying zero-pixels). Here, the word "zero-pixels" refers to pixels which have zero pixel values. As a result, unlike the ordinary iterative algorithms such as ART and EM algorithm, this new class of iterative algorithms can automatically estimate the OS during image reconstruction. When this concept is combined with the EM iterative reconstruction algorithm, it was shown that the resulting algorithm takes the form of alternating the following two substeps [15]. The first substep is the regular iteration step of EM algorithm, and the second substep is the thresholding operation called the hard/soft thresholding in the wavelet literature. The accuracy of zero-pixels identification is improved as the iteration proceeds, and the estimated OS approaches to the exact object boundary.

Recently, such algorithms have been investigated to solve general inverse problems, and are attracting attention of many researchers (e.g. [16, 17]). Our group also applied this class of iterative algorithms to 3D blood vessel reconstruction from limited number of projections [18] and PET/SPECT reconstruction [15]. In this paper, we use the same concept to estimate the OS in image reconstruction from truncated projection data. As shown later, this concept leads to automatically estimating the OS during the iteration and thereby reducing the DC-shift and low-frequency artifacts significantly.

3) Proposed reconstruction algorithm

In this section, we explain the proposed reconstruction algorithm. First, we note that the iterative algorithm here is essentially same as that in [15], though the target imaging application and the nature of projection data in this

paper are completely different from that in [15]. Let $\vec{x}=(x_1,...,x_n)$ denote the image vector and $\vec{y}=(y_1,...,y_m)$ denote the measured projection data. These two vectors are related to each other by the linear equation $A\vec{x}=\vec{y}$, where $A=\{a_{ij}\}$ is the $m\times n$ system matrix. Then, the proposed cost function for image reconstruction is expressed as

$$f(\vec{x})=L(\vec{x})+\beta T(\vec{x}), \tag{1}$$

Where $L(\vec{x})$ is the negative log-likelihood function, $T(\vec{x})$ is the distance function between the reconstructed image $\vec{x}$ and the null image, and β is the hyperparameter. The definition of $L(\vec{x})$ and $T(\vec{x})$ are given by

$$L(x)=\sum_{i=1}^{m}\left[\sum_{j=1}^{n}a_{ij}x_j-y_i\log\left(\sum_{j=1}^{n}a_{ij}x_j\right)\right] \tag{2}$$

$$T(\vec{x})=\sum_{j=1}^{n}s(x_j),\ \text{and}\ \ s(t)=\lim_{\varepsilon\to+0}|t|^{\varepsilon}\equiv\begin{cases}1 & t\neq 0\\ 0 & t=0\end{cases} \tag{3}$$

We derive the iterative reconstruction algorithm by using the majorization-minimization strategy same as that in [15]. The essential outline of the derivation is as follows. At each iteration k, we approximately majorize the non-separable part of the cost function $L(\vec{x})$ by a separable quadratic function $L(\vec{x};\vec{x}^{(k)})$ around $\vec{x}=\vec{x}^{(k)}$ as:

$$\begin{aligned}L(\vec{x};\vec{x}^{(k)}) &= L(\vec{x}^{(k)})+\nabla L(\vec{x})|_{\vec{x}=\vec{x}^{(k)}}(\vec{x}-\vec{x}^{(k)})^T+\frac{1}{2}\sum_{j=1}^{n}\frac{\sum_{i=1}^{m}a_{ij}}{x_j^{(k)}}(x_j-x_j^{(k)})^2\\ &=\sum_{j=1}^{n}\frac{\sum_{i=1}^{m}a_{ij}}{2x_j^{(k)}}(x_j-p_j)^2+C(\vec{x}^{(k)})\end{aligned} \tag{4}$$

$$p_j=\frac{x_j^{(k)}}{\sum_{i=1}^{m}a_{ij}}\sum_{i=1}^{m}\frac{a_{ij}y_i}{\sum_{j'=1}^{n}a_{ij'}x_{j'}^{(k)}}\ , \tag{5}$$

where $C(\vec{x}^{(k)})$ is the term independent of $\vec{x}$. Consequently, the final form of the separable surrogate cost function is given by

$$f(\vec{x};\vec{x}^{(k)})=\sum_{j=1}^{n}\beta[t_j(x_j-p_j)^2+s(x_j)]+C(\vec{x}^{(k)})\ \ \text{with}\ \ t_j=\frac{1}{2\beta x_j^{(k)}}\sum_{i=1}^{m}a_{ij} \tag{6}$$

At each iteration number k, the above cost function $f(\vec{x};\vec{x}^{(k)})$ is minimized instead of $f(\vec{x})$ to obtain the next iterate $\vec{x}^{(k+1)}$. Setting the partial derivative of Eq. (6) with respect to $\vec{x}$ equal to zero and then applying the non-negativity constraint $\vec{x}\geq 0$ yields the iteration formula given below by Eq. (7). The proposed iterative algorithm, which we call Th-OSEM (Threshold ordered subsets expectation maximization), is summarized as follows:

[STEP 1] (Initialization) Set the initial image as $\vec{x}^{(0)}=\varepsilon$ where $\varepsilon>0$ is a small positive number. Set the iteration number as $k\leftarrow 0$.

[STEP 2-1] (Majorization) Around the current iterate $\vec{x}^{(k)}$, $L(\vec{x})$ is (approximately) majorized using the separable function of Eq. (4) to get the surrogate cost function of Eq. (6).

[STEP 2-2] (Minimization) We minimize the cost function of Eq. (6) over $\vec{x}\geq 0$ to obtain the next iteration $\vec{x}^{(k+1)}$:

$$\vec{q}=\arg\min_{\vec{x}}f(\vec{x},\vec{x}^{(k)}),\ \ \vec{x}_j^{(k+1)}=\max(q_j,\delta) \tag{7}$$

where $\delta>0$ is a small value to guarantee that $x^{(k+1)}>0$.

[STEP 3] (Convergence check) Increment the iteration number as $k\leftarrow k+1$ and go to **[STEP 2-1]** until reaching to a stopping criterion.

The practical implementation of the proposed algorithm is simply described as follows. In **[STEP 2-1]**, the majorization substep is applied by computing $\vec{p}=(p_1,p_2,...,p_n)$ using Eq. (5) which is same as executing a single

iteration of the conventional OSEM algorithm. The minimization in **[STEP 2-2]** can be explicitly performed by the following thresholding function [15].

$$q_j = \begin{cases} 0 & p_j \le \sqrt{1/t_j} \\ p_j & elsewhere \end{cases}, \tag{8}$$

The Th-OSEM algorithm is executed as one substep of the conventional OSEM algorithm (Eq. (5)) followed by the pixel-by-pixel thresholding (Eq. (8)). The OSEM algorithm was used as a basic iterative algorithm to develop the proposed iterative method, because the non-negativity feature of the EM-based algorithms is helpful in regularizing the solution and estimating the OS more accurately. However, we note that the similar algorithms can be developed based on the other iterative algorithms such as ART and the conjugate gradient. The thresholding function in Eq. (8) has a large similarity to the well-known hard-thresholding operation in the wavelet denoising. This proposed algorithm belongs to a class of recently developed iterative reconstruction algorithms which use a sparsity constraint by employing a distance function based on the ℓ_1 / ℓ_0 norm [15 ~ 18]. A useful theoretical analysis of convergence can be found in [19].

4) Handling the hyperparameter β

In maximum *a posteriori* (MAP) reconstruction algorithms, the hyperparameter β in Eq. (1) is known as the regularization parameter which handles the strength of the prior term. In the proposed algorithm, β controls the size of the thresholding window as in Eq. (8). It is clear that β should be carefully selected, because, if it is assigned to a relatively large value, some low-frequency details in the reconstructed image will be lost due to the strong thresholding. In contrast, if β is relatively small, the merit of thresholding is small and the reconstruction algorithm behaves similar to the conventional iterative algorithms. We propose to use a dynamic value for this parameter by starting with a relatively large value (β_0) and then gradually decreasing it to zero according to the following rule.

$$\lim_{k\to\infty} \beta_k = 0 \quad \text{and} \quad \sum_{k=0}^{\infty} \beta_k = \infty \tag{9}$$

A simple setup to satisfy Eq. (9) is to use $\beta_k = \beta_0 /(1+k)$. This approach is based on the observation that, in the early iterations, a strong thresholding is required for the rough detection of the OS and a weak thresholding is preferred later to retrieve missing image details. We expect that the iteration converges to an approximate solution to the following optimization problem.

$$\text{Minimize} \quad T(\vec{x}) \quad \text{subject to} \quad A\vec{x} = \vec{y},\ \vec{x} \ge 0 \tag{10}$$

The rationale behind why the dynamic value of hyperparameter β_k should satisfy Eq. (9) is as follows. First, the left equation in Eq. (9) is necessary, because the value of β in the cost function of Eq. (1) should be close to zero for the solution minimizing $f(\vec{x})$ to coincide with the solution to the constrained problem of Eq. (10). On the other hand, the right equation in Eq. (9) intuitively means that the speed to decrease the value of β_k to zero should be sufficiently slow. This constraint is necessary, because, if the speed to decrease the value of β_k is too fast, the iteration is trapped at some point before reaching to the solution minimizing $T(\vec{x})$. For example, $\beta_k = \beta_0 /(1+k)$ satisfies this constraint, but $\beta_k = \beta_0 /(1+k)^2$ does not. We also note that the similar constraints have been used in the row-action maximum likelihood algorithm (RAMLA) for image reconstruction in emission tomography [20] and the gradient descent method with diminishing stepsize [21, p51].

3. Numerical results

1) The effect of OS

Simulation studies were performed to evaluate the effect of *a priori* knowledge of the OS to the quality of reconstructed images. These studies were performed using a single slice ($z = 0$) of the FORBILD thorax phantom with image matrix size of 512×512 pixels. The ROI was set to be a circle with a diameter of 160 pixels covering the cardiac region as shown in **Fig. 3**(a). The ROI position was selected such that the condition of Defrise is satisfied when the OS is close to the exact one (i.e. the ROI contains a small region outside the exact OS). The projection data were

computed with parallel-beam geometry for 512 radial bins and 512 views (over 180°), and the data were truncated manually such that only projection rays passing through the selected ROI are used for the reconstruction. Different selections of the OS constraint μ were applied that include exact OS knowledge, the case where the OS is known with different degrees of OS accuracy (110% ~ 150% larger than the exact OS) and the unknown OS. The "exact OS" means the true exact contour of the scanned object. The "110% OS" means the region inside the ellipse whose semi-axis length is 10% larger than that of the ellipse corresponding to the "exact OS". The definitions of "130% OS" and "150% OS" are similar (see **Fig. 3**(a)). The reconstruction was performed using the conventional OSEM algorithm with 8 subsets and 100 iterations for each setup. The implementation of the iterative reconstruction is as follows:

[Step 1] The image matrix $\vec{x}$ in the iterative algorithm is prepared such that it contains the whole object (not the ROI $\boldsymbol{\Omega}$ only) though only the ROI is the target to be reconstructed accurately.

[Step 2] The whole image matrix $\vec{x}$ is reconstructed by OSEM (section 3.1) or Th-OSEM (section 3.2) using only a set of projection data $\vec{y}$ which intersect the ROI $\boldsymbol{\Omega}$. When the OS is *a priori* known, after every iteration k, pixel values outside the OS are set to zeros.

[Step 3] Trim the reconstructed image matrix $\vec{x}$ to the small image which contains only the ROI $\boldsymbol{\Omega}$.

Reconstructed ROIs are shown in **Fig. 3** and the corresponding ROI central horizontal and vertical profiles are shown in **Fig. 4**. In **Fig. 3**, the reconstructed whole image matrix (512×512 pixels) was trimmed to the ROI image consisting of 512×300 pixels for display. It can be observed that improving the OS accuracy results in reduction of the DC-shift and low-frequency artifacts in the reconstructed images.

We note that, in the problem dealt with in this paper, 100 iterations with 8 subsets are reasonable choices, which were determined from the experimental optimization of iteration number. The explanation is as follows. The OSEM algorithm is normally used in PET/SPECT reconstruction. Though 100 iterations with 8 subsets are too many in PET/SPECT applications, the nature of the reconstruction problem in this paper differs from that in PET/SPECT with respect to the following point. In CT, unlike PET/SPECT imaging, the object normally contains low-contrast structures and the compressed gray scale (e.g. [0.94, 1.03] in **Fig. 3**) is used for image display to make the low-contrast structures visible. To recover the low-contrast structures with allowable small DC/low-contrast artifacts, more numbers of iterations are necessary compared to the case of PET/SPECT. So, we have carefully optimized the iteration number in the experimental study. In **Fig. 5**, we showed the profiles of the reconstructed images with 10, 20, 50,100, and 1000 iterations of the OSEM algorithm with 8 subsets. The results demonstrate that the DC/low-contrast artifacts still continue to decrease up to approximately 100 iterations, but only very small improvements were

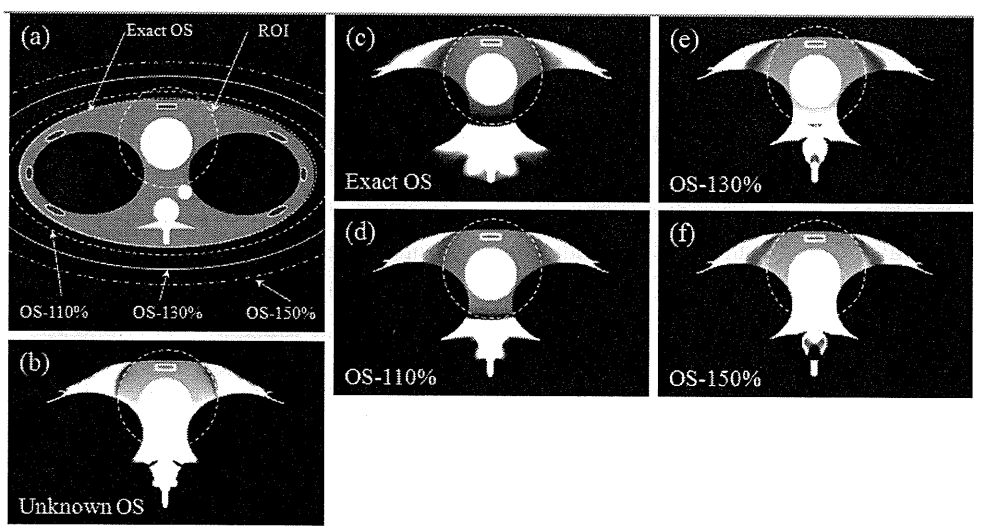

Fig. 3 (a) FORBILD thorax phantom ($z = 0$) and different OS setups, ROI reconstruction results with different OS degrees of accuracy, (b) OS is unknown, (c) OS is exact and (d) ~ (f) OS is known as the region that is larger than the exact OS. The display gray scale is [0.94, 1.03].

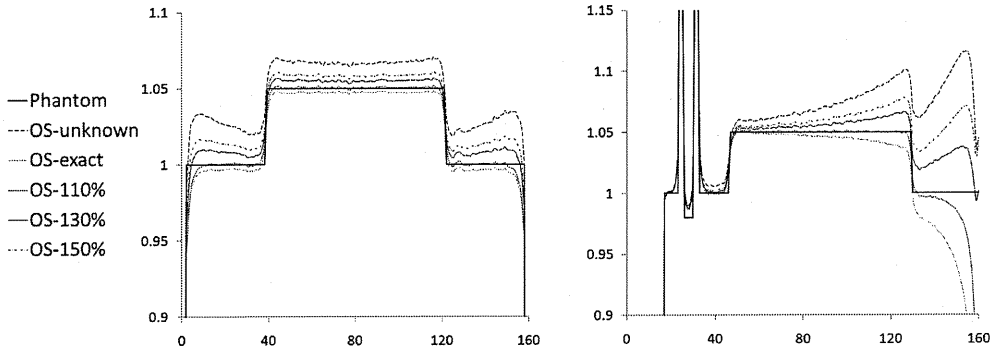

Fig. 4 Central horizontal (left) and vertical (right) profiles of ROI images shown in Fig. 3.

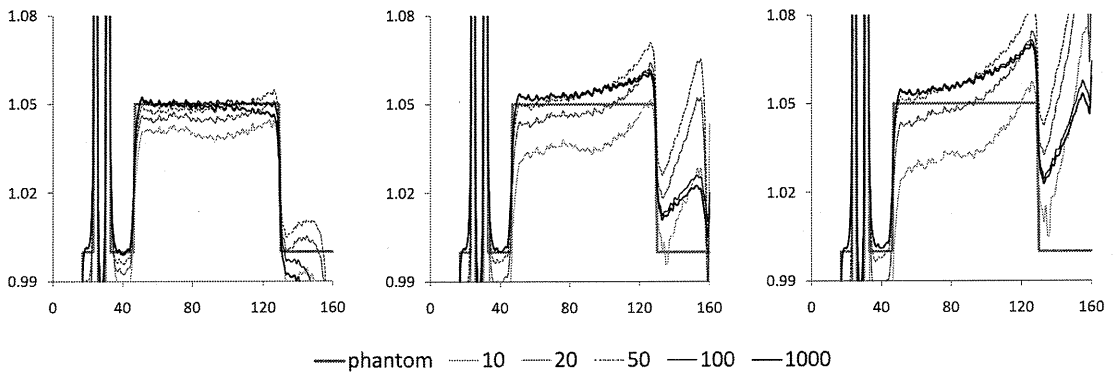

Fig. 5 Central vertical profiles of the reconstructed ROI images with different degrees of OS accuracy corresponding to 110% (left), 130% (middle) and 150% (right) using 10, 20, 50, 100, and 1000 iterations of OSEM algorithm with 8 subsets.

observed if we iterate more, from which we found that 10 or 20 iterations are not enough in the current problem. We also found that the necessary iteration number to achieve sufficient image quality did not depend very much on the OS accuracy as long as the OS is changed from "exact" to "150% OS". Furthermore, the convergence speed of the proposed algorithm with automatic OS estimation (detailed below in section 3.2) was only a bit slower compared to the cases where the OS is *a priori* known. From this experimental study (to determine the necessary iteration number) and the fact that the iterative algorithm with more than 100 iterations is not practical anymore, we performed all the simulation studies with 100 iterations.

2) Proposed iterative algorithm study

The ordered subsets version of the proposed algorithm, detailed above in section 2.3, was evaluated in comparison to the conventional OSEM algorithm. In this study, the FORBILD thorax phantom was modified by adding low-contrast hot/cold spots in the cardiac region to evaluate the effect of low-frequency artifacts. Other simulation parameters were similar to that in the previous study. The following three different scenarios were investigated. The first one assumes that the OS is exactly known (the ideal case) and reconstruction is done using the conventional OSEM algorithm. In the second and third scenarios, reconstruction is done using the OSEM and Th-OSEM with no *a priori* knowledge of the OS, respectively. Reconstructed ROIs for the noise free data and the data with added Poisson noise are shown in **Fig. 6** and the corresponding profiles are plotted in **Fig. 7**. The same image trimming as that in **Fig. 3** was used for display. It is clear that the proposed algorithm successfully reduces the DC-shift and low-frequency artifacts when the OS is unknown thanks to the automatic estimation of the OS.

From the reconstructed images in **Fig. 6** and the corresponding profiles in **Fig. 7**, it is noticed that the upper part of the ROI (close to the object boundary) suffers from less DC/low-frequency artifacts than the lower part (located at the center of object). In the followings we explain this phenomenon. It is known that the stability of inversion for

this reconstruction problem depends on the position of pixel inside the ROI. The inversion is more stable for the pixels located close to the upper part of the ROI (close to the object boundary), but the stability of inversion becomes unstable for the pixels located at the lower part (located at the center of object). This fact has been theoretically clarified by using the analytical continuation technique in [8] (please see **Fig. 5** of reference [8]). Here, we give an intuitive explanation for this variation in the stability from the view point of iterative reconstruction. For the pixels located at the upper part of the ROI, the boundary of OS is close so that the *a priori* knowledge that "the object is zero outside the OS" is quickly propagated to the pixels during iterative reconstruction, which result in better stability of inversion. However, for the pixels located at the lower part of the ROI, the closest OS is distant so that further iterations are necessary for the *a priori* knowledge to propagate to the reconstructed pixels, which result in worse stability.

From practical point-of-view, it is possible to correctly estimate a portion of the OS (corresponding to the top side of the object in the previous simulation study) from the truncated projection data directly by detecting the zero projection rays. However, by such simple method, the bottom side of the OS cannot be estimated from the truncated projection data. We verified that the top side of the OS alone is insufficient to get reconstruction comparable to **Fig. 6**(c). Moreover, such a simple method is not valid if the object is non-convex or the ROI is located completely inside the object (interior problem). A clinical example of this setup was studied here by modifying the phantom to simulate a female patient. In this setup, all the projection views suffer from the truncation in both the right and left portions. Even in this difficult setup, the solution is still unique if the OS is accurately known [8] . We simulated the same imaging setups as those of the previous studies and the results are presented in **Fig. 8**. Even with this challenging setup, the Th-OSEM behaves well and could reduce the artifacts in the reconstructed ROI.

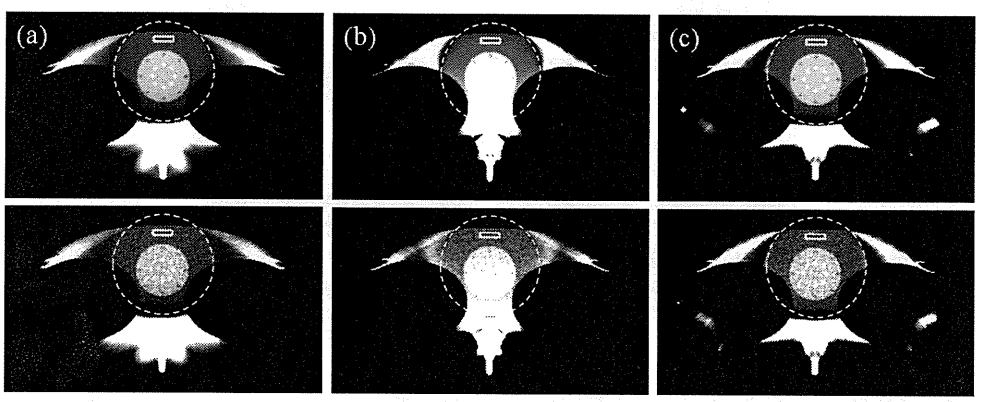

Fig. 6 Reconstructed ROIs by using (a) OSEM with the exact OS, (b) OSEM with the unknown OS and (c) Th-OSEM with the unknown OS. The top row shows reconstructions with noise free data and the bottom row shows reconstruction with added Poisson noise. The display gray scale is [0.95, 1.07].

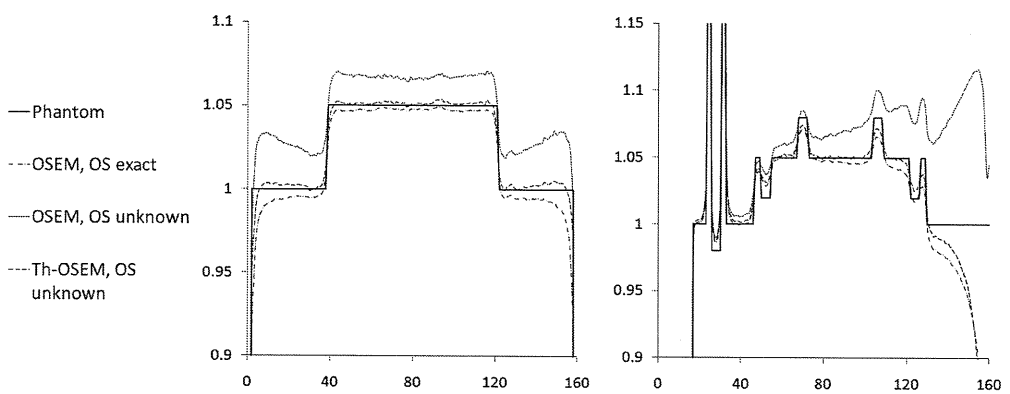

Fig. 7 Central horizontal (left) and vertical (right) profiles for ROI images shown in **Fig. 5** (top row).

In the simulation study to investigate the effect of OS accuracy on image quality (section 3.1), we assumed that the OS is known (with various degrees of accuracy) and used only the *a priori* knowledge that "the value of object is zero outside the known OS" (no *a priori* knowledge corresponding to the value of object inside the OS was used). On the other hand, in the simulation study to investigate the ability of the proposed algorithm (section 3.2), we assumed that the OS is unknown, because the purpose of this algorithm is to automatically estimate the OS. In other words, the proposed algorithm requires no *a priori* knowledge (except for the fact that the object has a finite support, which can be satisfied in every situation of CT imaging).

3) Real data

This study was done using a real data obtained from Siemens sensation 64 slice CT scanner using a 30×20×10 cm anthropomorphic chest phantom (QRM-thorax, QRM GmBH, Mohrendorf, Germany) shown in **Fig. 9**(d). The phantom consists of artificial lung lobes, shell of soft tissue equivalent material, tissue equivalent cardiac insert, and a spine insert, to which two water bottles were attached to represent the arms. Projection data was measured using the fan-beam geometry with 1,160 views (over 360°) and 672 detector channels. The projection data was rebinned into parallel-beam with 580 views (over 180°) and 672 radial bins. Image grid corresponding to the whole image was set to of 672×672 pixels and the ROI was selected as a circular region with a radius of 200 pixels covering the cardiac insert region. First, the FBP algorithm was used to reconstruct the whole object using the full scan data as shown in **Fig. 9**(a). Then a reconstruction was performed for ROI imaging using the OSEM and Th-OSEM

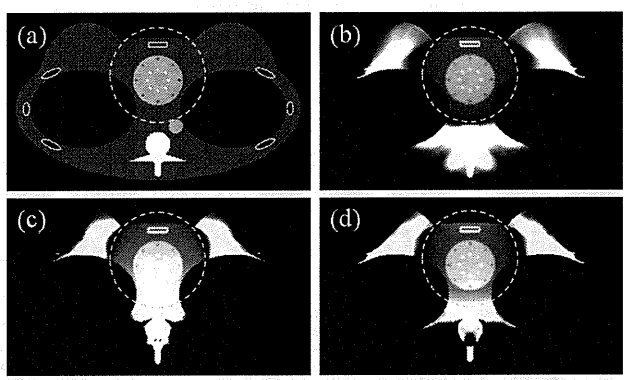

Fig. 8 (a) The modified phantom. Reconstructed ROIs using (b) OSEM with the exact OS, (c) OSEM with the unknown OS, and (d) Th-OSEM with the unknown OS. The display gray scale is [0.95 1.07].

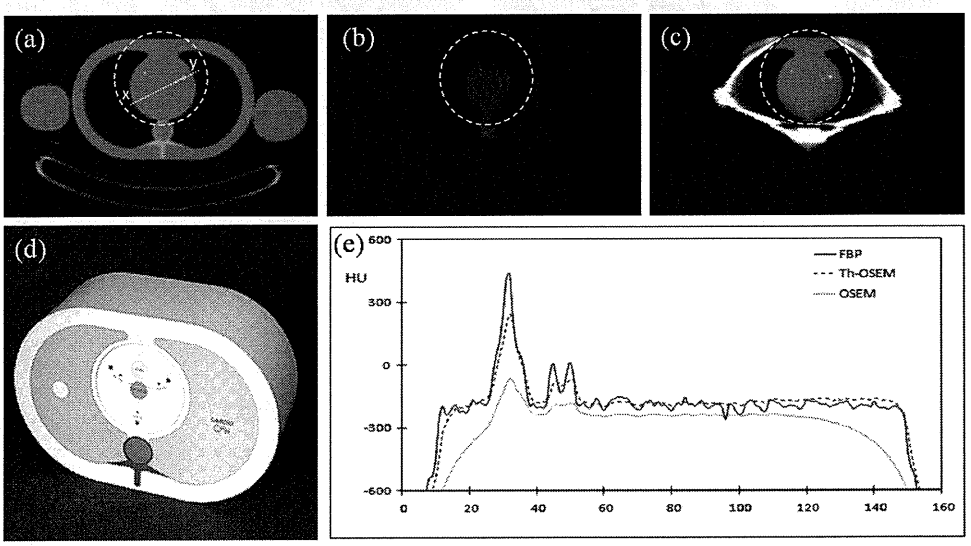

Fig. 9 Reconstructed images by using (a) FBP algorithm with the full scan, (b) OSEM with the ROI scan and (c) Th-OSEM with the ROI scan. The display window is set to [-480HU, 560HU]. (d) The original QRM-Thorax physical phantom (image from www.qrm.de). (e) Profiles corresponding to the white line segment (x-y) shown in (a).

algorithms with 16 subsets and 50 iterations without including the OS constraint. Reconstructed ROI images using OSEM and Th-OSEM are shown in **Fig. 9**(b) and (c), respectively. In **Fig. 9**, the reconstructed whole image matrix was trimmed to the ROI image consisting of 672×430 pixels for display. The results indicate a significant improvement in reducing the DC-shift and low-frequency artifacts when the Th-OSEM is employed.

4. Conclusions

The target of this work was to investigate the effect of OS constraint to the quality of reconstructed images from truncated projection data. This study implies that the lack of OS knowledge introduces DC-shift and low-frequency artifacts in the reconstructed images when the projection data is truncated. These artifacts decrease relative to the degree of OS accuracy. Moreover, we proposed an iterative algorithm that includes a sparsity constraint during the iteration in the form of thresholding function. This algorithm succeeded in reducing the artifacts thanks to its ability to automatically estimate the OS during reconstruction. The simulation results for noise free and noisy data show that the use of the proposed algorithm satisfactorily reduces the DC-shift and low-frequency artifacts even for the case where the OS is completely unknown. Moreover, the similar image improvements were achieved under more difficult configurations such as the non-convex object. The similar image improvements were also obtained by using the real data corresponding to the physical thorax phantom. The proposed algorithm is relatively simple and easy to be implemented and its extension to 3D reconstruction is also possible.

References

〔1〕 Brenner DJ, Hall EJ: Computed Tomography – An increasing source of radiation exposure. N Engl J Med **357**: 2277-2284, 2007

〔2〕 Lewitt RM: Processing of incomplete measurement data in computed tomography. Med Phys **6**: 412-417, 1979

〔3〕 Ogawa K, Nakajima M, Yuta S: A reconstruction Algorithm from Truncated Projections. IEEE Trans Med Imag **3**: 34-40, 1984

〔4〕 Ohnesorge B, Flohr T, Schwarz K et al: Efficient correction for CT image artifacts caused by objects extending outside the scan field of view. Med Phys **27**: 39-46, 2000

〔5〕 Zhang B, Zeng GL: Two-dimensional iterative region-of-interest (ROI) reconstruction from truncated projection data. Med Phys **34**: 935-944, 2007

〔6〕 Noo F, Clackdoyle R, Pack JD: A two-step Hilbert transform method for 2D image reconstruction. Phys Med Biol **49**: 3903-3923, 2004

〔7〕 Pan X, Zou Y, Xia D: Image reconstruction in peripheral and central regions-of-interest and data redundancy. Med Phys **32**: 673-684, 2005

〔8〕 Defrise M, Noo F, Clackdoyle R et al: Truncated Hilbert transform and image reconstruction from limited tomographic data. Inverse Problems **22**: 1037-1053, 2006

〔9〕 Kudo H, Courdurier M, Noo F et al: Tiny *a priori* knowledge solves the interior problem in computed tomography. Phys Med Biol **53**: 2207-2231, 2008

〔10〕 Ye Y, Yu H, Wei Y et al: A general local reconstruction approach based on a truncated Hilbert transform. Int J Biomed Imaging **2007**: Article ID 63634, 8 pages, 2007

〔11〕 Gregoriou GK, Tsui BMW, Gullberg GT: Effect of truncated projections on defect detection in attenuation-compensated fanbeam cardiac SPECT. J Nucl Med **39**: 166-175, 1998

〔12〕 Zeniya T, Watabe H, Sohlberg A et al: 3D-OSEM reconstruction from truncated data in pinhole SPECT. Conference Record of 2007 IEEE Medical Imaging Conference: Paper No. M25-1, 2007

〔13〕 Natterer F: The Mathematics of Computerized Tomography. SIAM, Philadelphia, 2001

〔14〕 Donoho DL: Compressed sensing. IEEE Trans Inf Theory **52**: 1289-1306, 2006

〔15〕 Mameuda Y, Kudo H: New anatomical-prior-based image reconstruction method for PET/SPECT. Conference Record of 2007 IEEE Medical Imaging Conference: Paper No. M23-2, 2007

〔16〕 Leng S, Tang J, Zambelli J et al: High temporal resolution and streak-free four-dimensional cone-beam computed tomography. Phys Med Biol **53**: 5653-5673, 2008

〔17〕 Trzasko J, Manduca A: Highly undersampled magnetic resonance image reconstruction via homotopic ℓ_0-minimization. IEEE Trans Med Imag **28**: 106-121, 2009

〔18〕 Li M, Yang H, Kudo H: An accurate iterative reconstruction algorithm for sparse objects: application to 3D blood-vessel reconstruction from a limited number of projections. Phys Med Biol **47**: 2599-2609, 2002

〔19〕 Daubechies I, Defrise M, De Mol C: An iterative thresholding algorithm for linear inverse problems with a sparsity constraint. Comm Pure Appl Math **57**: 1413-1457, 2004

〔20〕 Browne J, De Pierro AR: A row-action alternative to the EM algorithm for maximizing likelihoods in emission tomography. IEEE Trans Med Imag **15**: 687-699, 1996

〔21〕 Bertsekas DP: Nonlinear Programming. Athena Scientific, 1995

物体境界未知下におけるトランケーションCT投影データからの逐次近似法による関心領域画像再構成

イサム A. ラシド[*1] 工藤博幸[*1] フレデリック ヌー[*2]

[*1] 筑波大学大学院システム情報工学研究科コンピュータサイエンス専攻
[*2] ユタ大学放射線科

要旨：本論文では，トランケーションされたCT投影データからの画像再構成を取り扱う．X線を関心領域（ROI）のみに照射してROI画像を撮影するROIイメージングでは，投影データがトランケーションされ画像再構成は解が一意に定まりにくい難しい問題となる．最近開発された微分逆投影（DBP）の理論によりROIのサイズと配置によってはトランケーションされた投影データから厳密な画像再構成が可能な場合があることが示されたが，物体境界が事前に既知であることが前提となっている．しかし，実際のイメージング状況では物体境界が正確にわからない場合が多い．本論文では，(1) トランケーションされた投影データからの画像再構成において事前情報として用いる物体境界の精度と再構成画像のアーティファクトの関係を評価すること，(2) 逐次近似画像再構成の反復計算の過程において物体境界を自動推定しアーティファクトを低減する新しい画像再構成法を提案すること，の2つを目的とする．新しい手法では，画像再構成のコスト関数に画像のL0ノルムを加えることで物体境界の推定を実現している．シミュレーション実験と実データによる実験を行い，提案手法を用いることによりアーティファクトが大幅に低減できることを示す．

キーワード：トモグラフィ，画像再構成，ROIイメージング，トランケーション投影データ，物体境界
Med Imag Tech **27**(5): 321-331, 2009

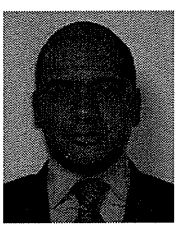

Essam A. Rashed（イサム ラシド）
Received his B.Sc. in scientific computing (with honors) and M.Sc. in computer science in 1998 and 2002 from Suez Canal Univ., Egypt, respectively. Now, he is with the doctoral program in systems and information engineering, Univ. of Tsukuba. His research interests include computed tomography and medical image processing. He is a winner of the Egyptian Government national scholarship (2006) and JAMIT best presentation award (2008). He is a member of IEEE NPSS and JAMIT.

Frédéric Noo（フレデリック ヌー）
Frédéric Noo, PhD., is a Tenured Associate Professor of Radiology at the University of Utah, where he joined the Utah Center for Advanced Imaging Research (UCAIR) in 2001. His specialty is x-ray computed tomography on which he described 126 original contributions in various journals and at conferences.

工藤博幸（くどう ひろゆき）
1985年東北大・工・通信卒．1990年同大大学院博士課程了．現在，筑波大・システム情報・教授．1990年電子情報通信学会論文賞，1991年・2001年・2006年・2008年日本医用画像工学会論文賞，2006年・2008年国際雑誌『Inverse Problems』High Lights，2008年国際雑誌『Physics in Medicine and Biology』High Lights受賞．工博．CTとPETを中心とした医用イメージング，画像処理の研究に従事．IEEE，電子情報通信学会，各会員．2008年にCTの未解決問題であるInterior Problemの安定な厳密解法を発見し，これに関する2つの論文が国際雑誌『Physics in Medicine and Biology』と『Inverse Problems』の2008 High Lightsを受賞した．

* * *

articles

molecular pharmaceutics

Nitroxyl Radicals for Labeling of Conventional Therapeutics and Noninvasive Magnetic Resonance Imaging of Their Permeability for Blood–Brain Barrier: Relationship between Structure, Blood Clearance, and MRI Signal Dynamic in the Brain

Zhivko Zhelev,[†] Rumiana Bakalova,*[,†] Ichio Aoki,[†] Ken-ichiro Matsumoto,[‡] Veselina Gadjeva,[§] Kazunori Anzai,[‡] and Iwao Kanno[†]

Department of Biophysics, Molecular Imaging Center, and Center for Heavy-ion Particle Therapy, National Institute of Radiological Sciences, 4-9-1 Anagawa, Inage-ku, Chiba 263-8555, Japan, and Department of Chemistry and Biochemistry, Trakia University, Stara Zagora, Bulgaria

Received September 24, 2008; Revised Manuscript Received January 7, 2009; Accepted January 9, 2009

Abstract: The present study describes a novel nonradioactive methodology for *in vivo* noninvasive, real-time imaging of blood–brain barrier (BBB) permeability for conventional drugs, using nitroxyl radicals as spin-labels and magnetic resonance imaging (MRI). Two TEMPO-labeled analogues (SLENU and SLCNUgly) of the anticancer drug lomustine [1-(2-chloroethyl)-3-cyclohexyl-1-nitrosourea] were synthesized, using a substitution of the cyclohexyl part with nitroxyl radical. Nonmodified nitroxyl radical TEMPOL was used for comparison. The nitroxyl derivatives were injected intravenously in healthy mice via the tail vein, and MR imaging of the brain was performed on a 7.0 T MRI. The MRI signal dynamic of SLENU and SLCNUgly followed the same kinetics as nonmodified TEMPO radical. SLENU and SLCNUgly were rapidly transported and randomly distributed in the brain tissue, which indicated that the exchange of cyclohexyl part of lomustine with TEMPO radical did not suppress the permeability of the anticancer drug for BBB. The selected nitroxyl derivatives possessed different hydrophobicity, cell permeabilization ability, and blood clearance. Based on these differences, we investigated the relationship between the structure of nitroxyl derivatives, their half-life in the circulation, and their MRI signal dynamic in the brain. This information was important for estimation of the merits and demerits of the described methodology and finding pathways for overcoming the restrictions.

Keywords: Nitroxyl radicals; lomustine; magnetic resonance imaging; electron-paramagnetic resonance imaging; blood–brain barrier permeability

Introduction

The nitroxyl radicals are well-known from electron-paramagnetic resonance (EPR) studies.[1−6] In 1984, it was reported that nitroxyl radicals possess comparatively high T_1 contrast properties and could be also applied in magnetic resonance imaging (MRI).[2,7] The nitroxyls are small molecules, sensitive to the reduction status of biological samples, and their use in life science research is limited predominantly to tissue oxygen and redox mapping *in vitro* and *in vivo*.[3−6,8−13] The paramagnetic nitroxyl radical could be reduced to diamagnetic hydroxylamine with a loss of EPR signal or ^{1}H-MRI relaxation time and thus serve as a reduction sensor. However, the diamagnetic hydroxylamine

* Author to whom correspondence should be addressed. Rumiana Bakalova, PhD, Department of Biophysics, Molecular Imaging Center, National Institute of Radiological Sciences (NIRS), 4-9-1 Anagawa, Inage-ku, Chiba 263-8555, Japan. Tel: +81-43-206-4067. Fax: +81-43-206-3276. E-mail: bakalova@nirs.go.jp; ra_bakalova@yahoo.com.

† Department of Biophysics, Molecular Imaging Center, National Institute of Radiological Sciences.

‡ Center for Heavy-ion Particle Therapy, National Institute of Radiological Sciences.

§ Trakia University.

(1) Griffeth, L. K.; Rosen, G. M.; Rauckman, E. J.; Drayer, B. P. Pharmacokinetics of nitroxide NMR contrast agents. *Invest. Radiol.* **1984**, *19*, 553–562.

10.1021/mp800175k CCC: $40.75
Published on Web 02/10/2009